



Cite this: *Nanoscale*, 2018, **10**, 11553

Enhanced exciton emission behavior and tunable band gap of ternary $W(S_xSe_{1-x})_2$ monolayer: temperature dependent optical evidence and first-principles calculations†

Huimin Sun,^a Junyong Wang,^a Fang Wang,^a Liping Xu,^a Kai Jiang,^a Liyan Shang,^a Zhigao Hu^{*,a,b} and Junhao Chu^a

Up to date, the electronic and optical properties of WS_2 and WSe_2 have been widely explored. However, the synthesis and characterization of their ternary alloy nanosheets have been rarely reported. Here, we fabricated single layer $W(S_xSe_{1-x})_2$ nanosheets by a one-step chemical vapor deposition (CVD) method. It is demonstrated that exciton emission behavior of single layer $W(S_xSe_{1-x})_2$ nanosheets ($0 \leq x \leq 1$) can be remarkably tuned by changing the sulfur content. The theoretical calculations proved that single layer $W(S_xSe_{1-x})_2$ alloy has a direct gap, and the band gap can be tuned by the sulfur content, which is in accordance with the spectral experiments. Moreover, we present temperature-dependent photoluminescence (PL) measurements in monolayers of $W(S_xSe_{1-x})_2$ alloys from 80 K to 320 K. The neutral exciton (X) and charged exciton (trion, T) can be observed at all measured temperatures. In sulfur-rich ternary $W(S_xSe_{1-x})_2$ alloys, the trion dominates the PL spectra at low temperatures while the exciton dominates the PL spectra at higher temperatures. In selenium-rich ternary alloys, however, the exciton is dominant in PL spectra at all measured temperatures. As the sulfur content gradually increases, the intensity ratio of the trion to exciton becomes dramatically larger. There is an obvious upward trend of the trion intensity in $W(S_xSe_{1-x})_2$ monolayers, which results from the significant growth of the two-dimensional electron gas (2DEG) concentration. On the other hand, the strong exciton–trion coupling mediated by an optical phonon also contributes to this improvement. These results indicate that exciton emission behavior of $W(S_xSe_{1-x})_2$ monolayers is controllable with the sulfur content. It highlights the importance of further detailed characterization on exciton features in ternary alloy nanosheets, and can enable spectral tunability for potential optoelectronic applications.

Received 3rd March 2018,

Accepted 30th May 2018

DOI: 10.1039/c8nr01823e

rsc.li/nanoscale

1 Introduction

Two-dimensional (2D) layered transition metal dichalcogenides (TMDCs) have drawn widespread research interest as a new class of atomically thin semiconductors due to the underlying physics and promising applications in photonics, optoelectronics and the development of valleytronics.^{1–6} As for the further study on 2D TMDC systems, researchers have

shifted their focus from the synthesis to the modification of 2D materials, aiming to create high performance semiconductor optoelectronic devices by manipulating their electronic structures.^{7–10} Semiconductor monolayer (ML) TMDCs have shown a direct band gap transition with strong photoluminescence (PL), demonstrating strong spin and valley coupling, which makes them an exciting class of 2D materials for future optoelectronic applications.^{11–14} Alloying 2D materials, stacking 2D materials vertically or growing lateral TMDC heterostructures and controlling the thickness of 2D materials are three main approaches to realize precise modulation of the band gap for TMDCs.¹⁵ To date, lots of TMDC alloys and heterostructures with variable chemical compositions have been synthesized to explore the electronic and optical properties of two-dimensional semiconductors.^{16–22} Ternary materials provide us with a more straightforward way to control the band gap by tuning the stoichiometry ratio of

^aKey Laboratory of Polar Materials and Devices (MOE) and Technical Center for Multifunctional Magneto-Optical Spectroscopy (Shanghai), Department of Electronic Engineering, East China Normal University, Shanghai 200241, China.

E-mail: zghu@ee.ecnu.edu.cn; Fax: +86-21-54345119; Tel: +86-21-54345150

^bCollaborative Innovation Center of Extreme Optics, Shanxi University, Taiyuan, Shanxi 030006, China

†Electronic supplementary information (ESI) available. See DOI: 10.1039/c8nr01823e

each element. Benefiting from a variety of candidates, the band gap of ternary materials can be tuned within a wide range. In monolayers of TMDCs the bottom of the conduction band and the top of the valence band are located at the 2D hexagonal Brillouin zone. The confinement to a single layer leads to strong many-body effects mediated by Coulomb interactions. In the TMDC monolayers, excitons, bound electron–hole pairs exhibit very high binding energies of a few hundred meV,^{23–25} which leads to their stability at room temperature. Temperature variation has an important influence on the lattice vibration and the nature of excitons in TMDC monolayers. Amit *et al.* and Philipp *et al.* reported the variation of the Raman modes with temperature from chemical vapor deposited monolayer MoS₂, MoSe₂, WS₂ and WSe₂.^{26,27} Humberto *et al.* and Jadcak *et al.* reported the evolution of the PL emissions with temperature for monolayer MoS₂, MoSe₂, WS₂ and WSe₂.^{28,29} Therefore, it is of fundamental importance to experimentally clarify the influences of temperature and components for exciton transitions and lattice vibrations in ternary monolayer TMDCs.

Mouri and co-workers used n-type or p-type dopants to tune the PL of MoS₂ monolayers, and the PL intensity of the MoS₂ monolayer could be drastically decreased or increased, respectively.³⁰ Feng and co-workers studied the variation of PL characteristics from a MoS₂ monolayer through hybridization with graphene quantum dots.³¹ Han *et al.* investigated the PL characteristics of WSe₂ doped with Cy₃/p-DNA, creating a sensitive optical biosensing material.³² However, the nature of excitons observed in different energy regions and the lattice vibration modes of such ternary alloy nanosheets have been rarely reported to date. The temperature dependence of the neutral and charged exciton emission behaviour in monolayer W(S_xSe_{1-x})₂ will impact the fundamental understanding of existing and future experiments on valley excitons in ternary TMDC semiconductors. This aspect of 2D exciton physics helps to reveal the origin of the unexpected values for excitons and trions, and open the way for the transition of correlated excitonic states in TMDC crystals. The ability to uncover this character will contribute to the development of potential electronic and optoelectronic applications of atomically thin TMDC materials.

In order to explore the electron–phonon interaction of chalcogenide layered materials, we performed a systematic investigation of Raman spectra and PL spectra in single-layer W(S_xSe_{1-x})₂ alloy nanosheets (0 ≤ x ≤ 1) in the temperature range from 80 K to 320 K. With the aid of theoretical calculations, it was found that single-layer W(S_xSe_{1-x})₂ alloy is a direct-gap semiconductor and the band gap increases with the sulfur content. Moreover, the intensity ratio of trion to exciton increases with the sulfur content in ternary W(S_xSe_{1-x})₂ alloys in the high-temperature range. The observed sensitivity of the exciton emission to temperature in monolayer W(S_xSe_{1-x})₂ and band gap variation further indicates the potential of this atomically thin TMDC material for various applications, such as electronics and optoelectronics.

2 Experimental

2.1 Chemical vapor deposition of single layer W(S_xSe_{1-x})₂ alloys

We have synthesized monolayer W(S_xSe_{1-x})₂ by using the chemical vapor deposition (CVD) method containing two heating zones (as shown in ESI Fig. S1†). In a typical experiment, selenium (Se) powder (99.99%, Sigma-Aldrich) and sulfur (S) powder (99.9%, Sigma-Aldrich) were placed in the first zone of the furnace at the upstream end, tungsten oxide (WO₃) powder (99.998%, Alfa Aesar) was placed inside the quartz tube in the second zone. Clean 300 nm SiO₂/Si wafers were then placed face down on the crucible containing the WO₃ powder. After loading all the precursors, the tube was sealed and purged with an Ar/H₂ flow. The temperature of the second zone was raised to 800 °C with a heating ramp of 16 °C min⁻¹ and the deposition took place at 800 °C for 15 min. At the same time, the temperature of the first zone also reached 280 °C so as to evaporate the selenium and sulfur mixture powders. After the deposition, the furnace was cooled naturally to room temperature. During the entire growth process, the Ar/H₂ flow rate was maintained at 60 sccm.

2.2 Materials characterization

Chemical vapor deposited monolayers of W(S_xSe_{1-x})₂ were characterized using optical microscopy, atomic force microscopy (AFM), Raman spectroscopy and energy dispersive X-ray spectroscopy (EDS) elemental analysis. Surface morphologies of W(S_xSe_{1-x})₂ alloys were investigated by atomic force microscopy (AFM: Digital Instruments Icon, Bruker) with ScanAsyst modes. Energy dispersive X-ray spectroscopy (EDS) based on SEM was also conducted, showing the intrinsic sulfur molar content of the alloys. The temperature dependent PL and Raman experiments were carried out using a Jobin–Yvon LabRAM HR Evolution spectrometer and a THMSE 600 heating/cooling stage (Linkam Scientific Instruments) in the temperature range from 80 K to 320 K with a resolution of 0.1 K. The alloy nanosheets were excited by the 532 nm line of an Ar laser with the output power of ~5 mW and recorded in back-scattering geometry with a resolution of better than 1 cm⁻¹. An air-cooled CCD (–70 °C) with a 1024 × 256 pixel front-illuminated chip was used to collect the scattered signal dispersed on an 1800 grooves per mm grating for Raman and a 300 grooves per mm grating for PL. The laser beam was focused through a 50× microscope with a working distance of 18 mm to avoid the possible heating effect of the laser on the monolayer samples.

2.3 Computational details

The density functional theory (DFT) and virtual-crystal approximation (VCA) calculations were performed with plane-wave pseudopotentials from the calculation method of quantum mechanics.^{33–35} To model the ternary W(S_xSe_{1-x})₂ (0 ≤ x ≤ 1) alloy nanosheets of the generic composition, we have adopted

the VCA, which implies preserving the same crystalline unit cells as the binary compounds, such as WS_2 and replacing the non-metallic element sulfur with a virtual selenium atom.³⁶ The generalized gradient approximation (GGA) for the exchange–correlation term was employed, and the functional was adopted for structure optimization and band gap calculation.³⁷ The selected pseudopotential was Ultrasoft Pseudopotentials. A planewave cutoff energy of 450 eV and a $10 \times 10 \times 1$ grid of Monkhorst–Pack points were employed to ensure good convergence of the computed structures and energies. Geometry optimization was determined using the Broyden–Fletcher–Goldfarb–Shenno (BFGS) minimization technique, with thresholds of converged structure of energy change per atom smaller than 5×10^{-6} eV per atom, and displacement of atoms during geometry optimization no more than 5×10^{-4} Å. The tolerance in the self-consistent field (SCF) calculation was 1.0×10^{-6} eV per atom. All calculations were carried out using a 1×1 supercell with vacuum thickness not smaller than 25 Å.

3 Results and discussion

3.1 Morphology analysis and Raman spectra of single layer $\text{W}(\text{S}_x\text{Se}_{1-x})_2$

Fig. 1(a) shows an optical microscopy image of a triangular shaped single layer $\text{W}(\text{S}_x\text{Se}_{1-x})_2$ nanosheet with the lateral dimension of $\sim 30 \mu\text{m}$. The formation of triangular shaped TMDC nanosheets and the growth mechanism mainly depend on three factors: (i) gas flow rate, (ii) substrate temperature, (iii) the ratio of M and X powder (where $M = \text{W}$ and $X = \text{Se}, \text{S}$ etc.).²⁶ In this work, the band gap of the alloy nanosheets was mainly tuned by systematically controlling the ratio of sulfur and selenium powders. Further AFM images and height profiles were analyzed to confirm the number of layers presented in the sample. Fig. 1(b, c) show the typical AFM measurement results, which indicate the thickness of nanosheets ~ 0.75 nm and confirm the single layer nature of $\text{W}(\text{S}_x\text{Se}_{1-x})_2$.

Raman spectroscopy was performed to investigate the structural evolution and optical characteristics of the as-grown

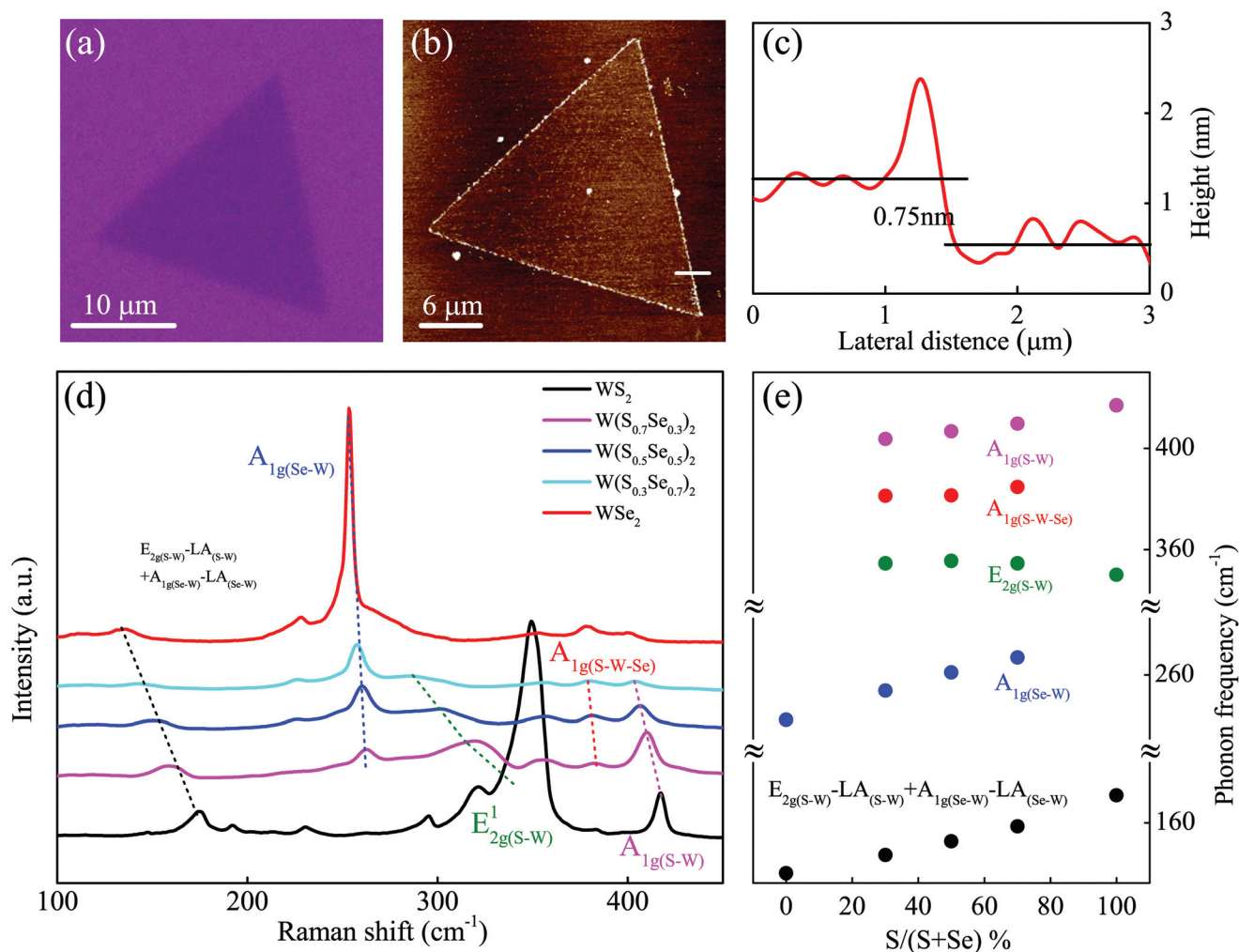


Fig. 1 Single layer $\text{W}(\text{S}_{0.7}\text{Se}_{0.3})_2$ alloy nanosheets: (a) optical microscopy image, (b) AFM image of $\text{W}(\text{S}_{0.7}\text{Se}_{0.3})_2$ alloy, (c) corresponding AFM height profile of single layer $\text{W}(\text{S}_{0.7}\text{Se}_{0.3})_2$ alloy, (d) Raman spectra and (e) phonon frequency shifts with increasing S molar content for $\text{W}(\text{S}_x\text{Se}_{1-x})_2$ alloys.

$W(S_xSe_{1-x})_2$ nanosheets. Fig. 1(d) shows the Raman spectra of single-layer $W(S_xSe_{1-x})_2$ alloys with sulfur molar contents from $x = 0$ up to $x = 1$ recorded at room temperature. A typical Raman spectrum of single-layer $W(S_xSe_{1-x})_2$ consists of five main phonon vibration modes, which can be assigned to the $A_{1g(s-w)}$ ($403.7\text{--}416.9\text{ cm}^{-1}$), $A_{1g(se-w)}$ ($253.7\text{--}262.5\text{ cm}^{-1}$), $A_{1g(s-w-se)}$ ($381.2\text{--}384.7\text{ cm}^{-1}$), $E_{2g(s-w)}$ ($350.1\text{--}354.6\text{ cm}^{-1}$), and $E_{2g(s-w)-LA(s-w)} + A_{1g(se-w)-LA(se-w)}$ modes ($134.8\text{--}173.7\text{ cm}^{-1}$). The normalized Raman spectra of the $W(S_xSe_{1-x})_2$ nanosheets with modulated compositions show an obvious phonon frequency shift and relative intensity evolution for the A_{1g} mode [Fig. 1(d)].

For binary WS_2 , the frequencies of the first-order Raman lines are equal to 416.9 cm^{-1} and 354.6 cm^{-1} . They are assigned to the out-of-plane A_{1g} and in-plane E_{2g} modes, respectively.^{38,39} As the sulfur content slightly decreases, we can identify additional features in the Raman spectra in the range of $370\text{--}450\text{ cm}^{-1}$. The presence of a selenium atom in the host lattice of WS_2 induces vibrations with out-of-plane weight in the vicinity of the A_{1g} mode, resulting in characteristic splitting into two Raman features denoted as $A_{1g(s-w)}$ and $A_{1g(s-w-se)}$ modes. The splitting is directly related to different distributions of the chalcogenide atoms within the $W(S_xSe_{1-x})_2$ layers. Based on their intensities, we have divided them into two groups.⁹ The first group, at lower frequencies, corresponds to the S–W–Se configuration, whereas the second group at higher frequencies is likely related to the S–W–S vibration.^{9,40} It is noteworthy that the 378 cm^{-1} and 400 cm^{-1} vibration modes from pure WSe_2 observed in Fig. 1(d) are different from the two splitting modes in $W(S_xSe_{1-x})_2$ alloys mentioned above. According to the existing studies of monolayer WSe_2 ,⁴¹ they were identified as $A_{1g(se-w)} + LA_{(se-w)}$ and $2A_{1g(se-w)} - LA_{(se-w)}$ vibration modes. As seen in Fig. 1(e), the $A_{1g(s-w)}$ and $A_{1g(s-w-se)}$ peaks evolve in a similar manner as a function of increasing sulfur content. The $A_{1g(s-w)}$ mode shows a strong resonance at 403.7 cm^{-1} for the WSe_2 -rich phase, which systematically shifts to a higher frequency (up to 416.9 cm^{-1}) with increasing intensity as the sulfur ratio increases. Additionally, another alloy peak, the $A_{1g(s-w-se)}$ mode, can be also observed in the $W(S_xSe_{1-x})_2$ alloy nanosheets, with the resonance frequency shifting from 381.2 cm^{-1} in the WSe_2 -rich phase to 384.7 cm^{-1} in the WS_2 -rich phase. Similarly, the $A_{1g(se-w)}$ mode follows the same trend and changes from a strong resonance at 253.7 cm^{-1} for the pure WSe_2 phase to 262.5 cm^{-1} for the WS_2 -rich phase. The $E_{2g(s-w)-LA(s-w)} + A_{1g(se-w)-LA(se-w)}$ mode, *i.e.*, the superposition of $E_{2g(s-w)-LA(s-w)}$ and $A_{1g(se-w)-LA(se-w)}$, also shows a systematic shift from 134.8 cm^{-1} for the WSe_2 -rich phase to 173.7 cm^{-1} for the WS_2 -rich phase, which matches well with the individual phonon frequency evolution of $E_{2g(s-w)}$ and $A_{1g(se-w)}$. Note that it is unique for $W(S_xSe_{1-x})_2$ alloy nanosheets. It is also worth noting that the $E_{2g(s-w)}$ mode remains at nearly the same frequency, with less than 4.5 cm^{-1} difference across the entire composition modulation range. There is little contribution from the $E_{2g(se-w)}$ mode, which could be attributed to the very weak $E_{2g(se-w)}$ mode and its weak coupling with the strong $E_{2g(s-w)}$ mode. The phonon fre-

quency variations with the sulfur content further confirm the expected structural and compositional evolution in the $W(S_xSe_{1-x})_2$ alloy nanosheets.

3.2 Temperature dependent Raman spectroscopy

Fig. 2(a)–(c) show the Raman shift as a function of temperature for the CVD grown $W(S_xSe_{1-x})_2$ nanosheet samples with $x = 0.7, 0.5, 0.3$, respectively. The Raman shifts as a function of temperature for pure WS_2 and WSe_2 are shown in ESI Fig. S2.† The spectra were measured from 80 K up to 320 K in steps of 20 K. Fig. 2(d)–(h) show the temperature dependence of the frequencies of the Raman-active $A_{1g(s-w)}$, $A_{1g(se-w)}$, $A_{1g(s-w-se)}$, $E_{2g(s-w)}$, and $E_{2g(s-w)-LA(s-w)} + A_{1g(se-w)-LA(se-w)}$ bands of monolayer $W(S_{0.7}Se_{0.3})_2$ samples. It clearly shows the downward shift in the main five Raman modes with increasing temperature in the single-layer $W(S_{0.7}Se_{0.3})_2$ alloy. The temperature coefficients of frequencies for the $A_{1g(s-w)}$, $A_{1g(se-w)}$, $A_{1g(s-w-se)}$, $E_{2g(s-w)}$, and $E_{2g(s-w)-LA(s-w)} + A_{1g(se-w)-LA(se-w)}$ modes from single-layer $W(S_{0.7}Se_{0.3})_2$ were found to be -0.01371 , -0.01013 , -0.00645 , -0.00759 and $-0.00575\text{ cm}^{-1}\text{ K}^{-1}$, respectively. In the single-layer $W(S_xSe_{1-x})_2$ alloy, it was found that the temperature coefficients of both $A_{1g(s-w)}$ and $A_{1g(se-w)}$ modes from single-layer $W(S_{0.7}Se_{0.3})_2$ are larger than those of the other three Raman modes. In the monolayer $W(S_{0.5}Se_{0.5})_2$ and $W(S_{0.3}Se_{0.7})_2$ samples, the Raman shifts show the same downward trend as the temperature increases as shown in ESI Fig. S3 and S4.† The phonon frequency can be calculated by fitting the Lorentzian functions for each mode as a function of temperature given by the following formula:⁴² $\omega(T) = \omega_0 + \chi T$, where ω_0 is the phonon frequency of the $A_{1g(s-w)}$, $A_{1g(se-w)}$, $A_{1g(s-w-se)}$, $E_{2g(s-w)}$, or $E_{2g(s-w)-LA(s-w)} + A_{1g(se-w)-LA(se-w)}$ vibration modes at zero Kelvin, and χ is the first order temperature coefficient of the vibration modes. The Raman modes $A_{1g(s-w)}$, $A_{1g(se-w)}$, $A_{1g(s-w-se)}$, $E_{2g(s-w)}$, and $E_{2g(s-w)-LA(s-w)} + A_{1g(se-w)-LA(se-w)}$ behave linearly in the temperature range from 80 K to 320 K. The slope of the fitted straight line depicts the temperature coefficient (χ). The calculated values of temperature coefficients and variations in phonon frequency as a function of temperature for different modes are shown in Table 1, which provides a summary of extracted temperature coefficients and frequency differences for single-layer $W(S_xSe_{1-x})_2$ nanosheets. In the $W(S_{0.7}Se_{0.3})_2$ alloy, $\Delta\omega$ values with temperature variation from 80 to 320 K were observed to be 2.28 cm^{-1} for $A_{1g(se-w)}$, 3.11 cm^{-1} for $A_{1g(s-w)}$, 1.82 cm^{-1} for $A_{1g(s-w-se)}$, 2.47 cm^{-1} for $E_{2g(s-w)}$, and 1.24 cm^{-1} for $E_{2g(s-w)-LA(s-w)} + A_{1g(se-w)-LA(se-w)}$ modes, respectively. For WS_2 , however, $\Delta\omega$ is observed to be 1.51 cm^{-1} for $E_{2g(s-w)}$, and 1.62 cm^{-1} for $A_{1g(s-w)}$, and in WSe_2 , $\Delta\omega$ is observed to be 1.55 cm^{-1} for $A_{1g(se-w)}$. The variations in phonon frequencies $\Delta\omega$ of ternary $W(S_xSe_{1-x})_2$ alloys are larger than those of the binary WS_2 and WSe_2 samples. The observed behavior may be due to the contribution from a double resonance phenomenon, which is active only in atomically thin sheets. The double resonance phenomenon includes phonon–phonon interactions and electron–phonon interactions. The phonon–phonon interaction involves a phonon decaying into lower-

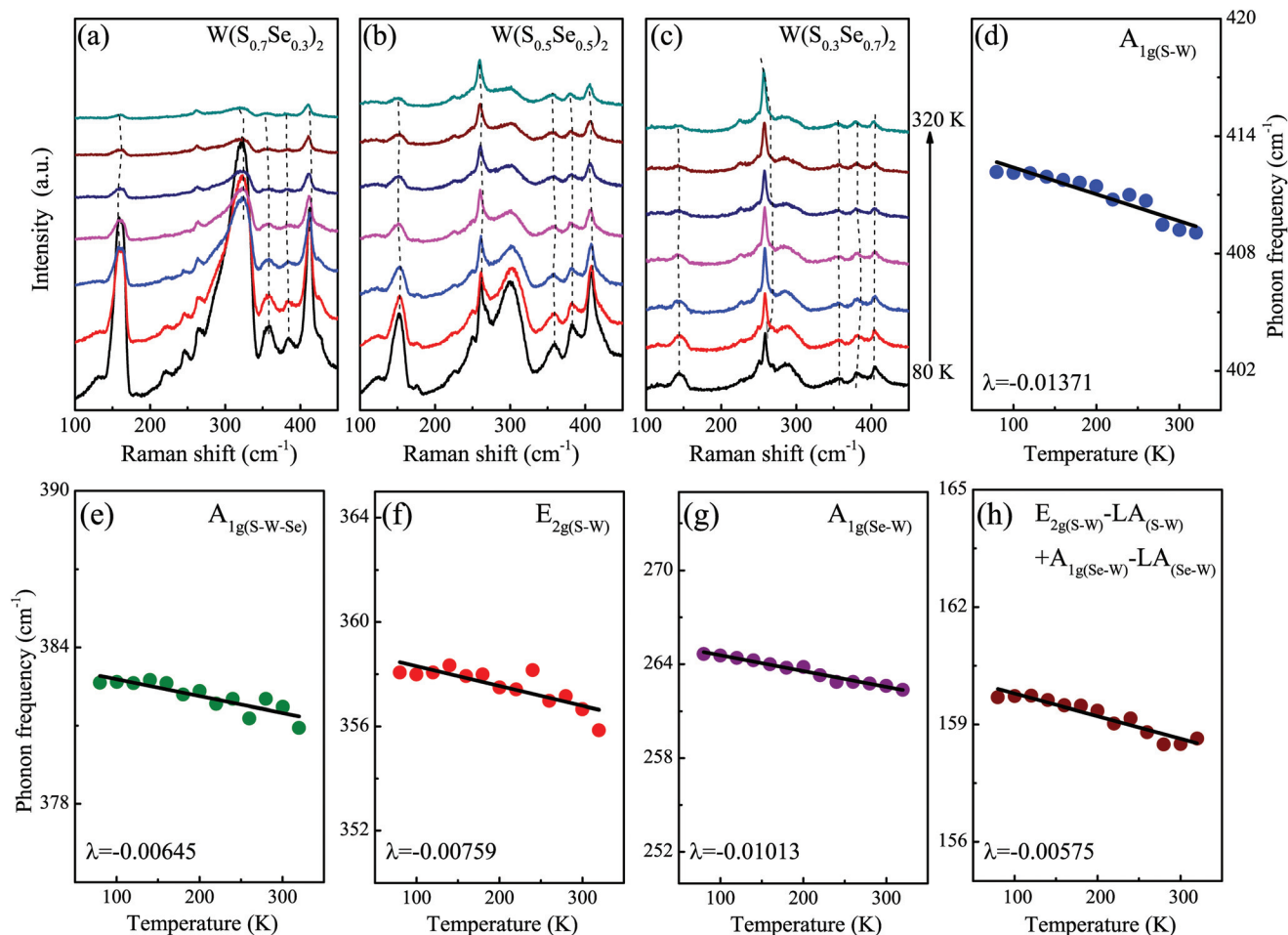


Fig. 2 Raman spectra as a function of temperature for single layer $W(S_xSe_{1-x})_2$ nanosheets: (a) $W(S_{0.7}Se_{0.3})_2$, (b) $W(S_{0.5}Se_{0.5})_2$, and (c) $W(S_{0.3}Se_{0.7})_2$. (d)–(h) Phonon frequencies of five main vibrational modes as a function of temperature for monolayer $W(S_{0.7}Se_{0.3})_2$ nanosheets.

Table 1 Main vibrational modes from Raman spectra as a function of temperature for chemical vapor deposited monolayer $W(S_xSe_{1-x})_2$ nanosheets with sulfur molar content from 0 to 1

Monolayer TMDC	Phonon modes	Temperature coefficient χ ($\text{cm}^{-1} \text{K}^{-1}$)	$\Delta\omega$ (cm^{-1})
WS_2	$E_{2g(S-W)}^1$	-0.00213	1.51
WS_2	$A_{1g(S-W)}$	-0.00768	1.62
$W(S_{0.7}Se_{0.3})_2$	$E_{2g-LA} + A_{1g-LA}$	-0.00575	1.24
$W(S_{0.7}Se_{0.3})_2$	$A_{1g(Se-W)}$	-0.01013	2.28
$W(S_{0.7}Se_{0.3})_2$	$A_{1g(S-W)}$	-0.01371	3.11
$W(S_{0.7}Se_{0.3})_2$	$A_{1g(S-W-Se)}$	-0.00645	1.82
$W(S_{0.7}Se_{0.3})_2$	$E_{2g(S-W)}^1$	-0.00759	2.47
$W(S_{0.5}Se_{0.5})_2$	$E_{2g-LA} + A_{1g-LA}$	-0.01374	3.34
$W(S_{0.5}Se_{0.5})_2$	$A_{1g(Se-W)}$	-0.01050	2.35
$W(S_{0.5}Se_{0.5})_2$	$A_{1g(S-W)}$	-0.01522	3.54
$W(S_{0.5}Se_{0.5})_2$	$A_{1g(S-W-Se)}$	-0.00985	2.63
$W(S_{0.5}Se_{0.5})_2$	$E_{2g(S-W)}^1$	-0.01508	3.54
$W(S_{0.3}Se_{0.7})_2$	$E_{2g-LA} + A_{1g-LA}$	-0.00631	1.97
$W(S_{0.3}Se_{0.7})_2$	$A_{1g(Se-W)}$	-0.01261	3.24
$W(S_{0.3}Se_{0.7})_2$	$A_{1g(S-W)}$	-0.01396	3.79
$W(S_{0.3}Se_{0.7})_2$	$A_{1g(S-W-Se)}$	-0.00701	2.07
$W(S_{0.3}Se_{0.7})_2$	$E_{2g(S-W)}^1$	-0.00221	2.83
WSe_2	$A_{1g(Se-W)}$	-0.00568	1.55

energy phonons, and the electron–phonon interaction results from a phonon generating an electron–hole pair. Moreover, the presence of a selenium atom in the host lattice of WS_2 induces vibrations in the phonon modes with the temperature, which is mostly due to the effect of anharmonicity and the influence from thermal expansion or volume contribution.

3.3 Photoluminescence spectra and band structures for $W(S_xSe_{1-x})_2$ alloy nanosheets

Fig. 3(a) shows the photoluminescence spectra of alloy nanosheets. The PL peak positions are continuously tunable from 644.05 nm (nearly pure WS_2) to 761.77 nm (nearly pure WSe_2) depending on the ratio of sulfur and selenium powders. To correlate the band gap energy with the sulfur content of the alloy nanosheets, we have approximated the band gap (E_g) using the PL emission peak position ($E_g = hc/\lambda$, where h is Planck's constant, c is the speed of light, and λ is the wavelength of the PL peak) and determined the composition using energy dispersive X-ray spectroscopy (EDS) elemental analysis. In Fig. 3(b), the plot of the band gap *versus* sulfur molar

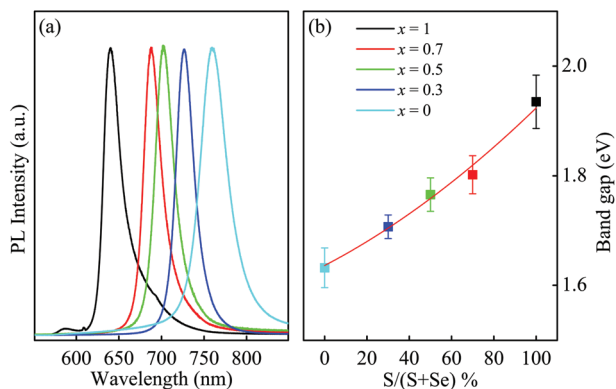


Fig. 3 (a) Photoluminescence spectra of $W(S_xSe_{1-x})_2$ monolayer nanosheets. (b) Optical band gap versus sulfur ratio in $W(S_xSe_{1-x})_2$ monolayers.

content shows an almost linear relationship, as expected since the band gap of ternary $W(S_xSe_{1-x})_2$ alloys is located between those of the binary WS_2 and WSe_2 semiconductors. These studies clearly demonstrate that the band gap of the alloy nanosheets can be tuned from pure WSe_2 to pure WS_2 by systematically controlling the ratio of sulfur and selenium powders. The band gap tunability in the $W(S_xSe_{1-x})_2$ alloy system can greatly enrich the 2D material family and enable spectral tunability for potential optoelectronic applications.

To better understand the observed composition-dependent light-emission behavior, we calculated the band structures of the monolayer $W(S_xSe_{1-x})_2$ alloys at different sulfur molar contents using the DFT method. As shown in Fig. 4(a–e), both the valence-band maximum (VBM) and conduction-band minimum (CBM) are located at the K point in the Brillouin zone, which is similar to other binary TMDCs.²⁸ The CBM and VBM at the K point are mainly due to tungsten d-orbitals, located in the middle of the S–W–Se layer sandwiches and relatively unaffected by interlayer coupling.

However, the CBM at $K-\Gamma$ and the VBM at Γ are due to combinations of the antibonding p_z -orbitals on the sulfur atoms and the d_{z^2} orbitals on tungsten atoms.⁴³ For bulk WS_2 , the electronic states involved in the indirect transition exhibit a strong interlayer coupling. For a monolayer, however, the indirect gap between these states is larger than the direct transition at K, thus making the material a direct band gap semiconductor.⁴⁴ In Fig. 4(f), it is shown that the direct band gap of the $W(S_xSe_{1-x})_2$ alloy nanosheets increases with increasing sulfur molar content, which agrees well with the experimental observations. Furthermore, the direct excitonic transition energy at the K point shows remarkable variation with the band gap shifting from 1.6 eV for the WSe_2 -rich phase to 1.8 eV for the WS_2 -rich phase. With the sulfur content decreasing, not only does the VBM at Γ point becomes lower with respect to the K point, but also the CBM at a midpoint between the K and Γ points becomes lower. As the content of

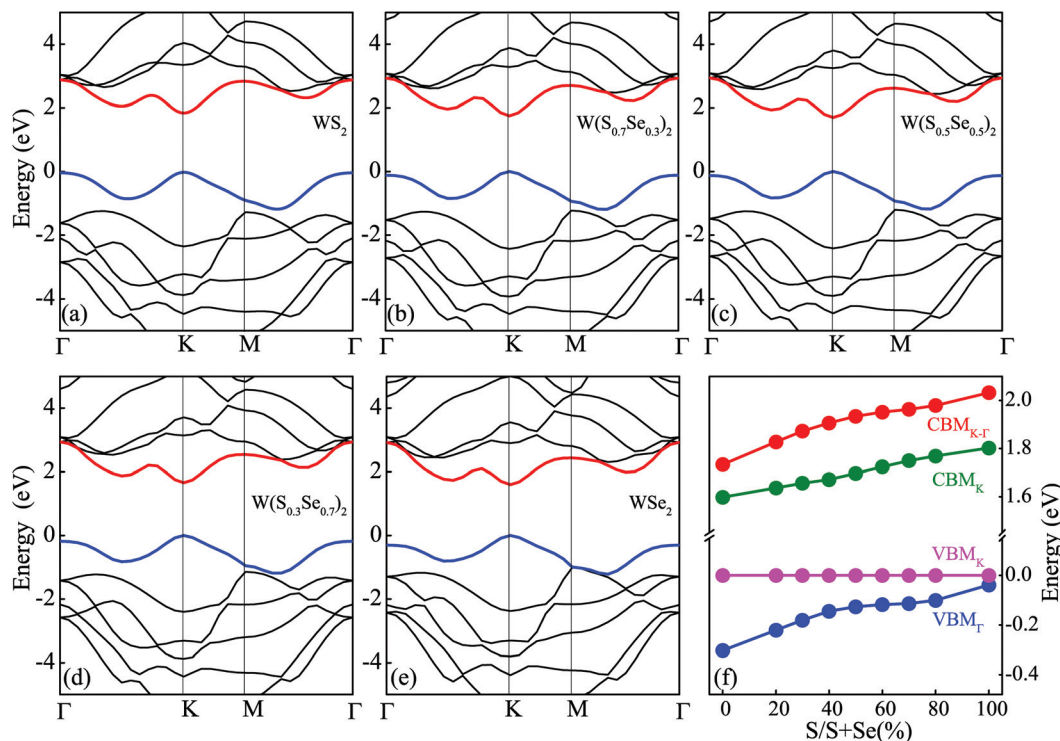


Fig. 4 The electronic band structures for $W(S_xSe_{1-x})_2$ alloy nanosheets: (a) WS_2 , (b) $W(S_{0.7}Se_{0.3})_2$, (c) $W(S_{0.5}Se_{0.5})_2$, (d) $W(S_{0.3}Se_{0.7})_2$, and (e) WSe_2 . (f) Variation of the VBM and CBM with respect to the sulfur molar ratio for $W(S_xSe_{1-x})_2$ alloy nanosheets. The parameters VBM_K and CBM_K refer to the local highest valence and lowest conduction states at the K point, VBM_Γ to the Γ point, and $CBM_{K-\Gamma}$ to the path $K-\Gamma$.

sulfur increases, the energy difference between the local maxima of the K and Γ points in the valence band (VB) decreases. Moreover, by varying the sulfur ratio from 0 to 1, the VBM at the Γ point shows a dramatic increase up to 0.26 eV involving p-d orbital coupling. Our DFT calculations estimated that $W(S_xSe_{1-x})_2$ alloys are 2D semiconductors with a direct gap in the visible spectral range. The band gap values of ternary $W(S_xSe_{1-x})_2$ alloys are located between the band gaps of binary WS_2 and WSe_2 . The band gap value increases obviously with increasing sulfur molar content, which is in accordance with the transition transformation observed in the experiments.

3.4 Temperature dependent photoluminescence spectroscopy

A schematic diagram of the direct K-K interband transition in the 2D hexagonal Brillouin zone between the conduction and valence bands of $W(S_xSe_{1-x})_2$ alloys is presented in Fig. 5(a). The strong spin-orbit coupling and lack of inversion symmetry lead to valley-contrasting strong spin splitting of the valence and conduction bands.⁴⁵⁻⁴⁷ We attribute the two split peaks to the neutral exciton (X, the higher-energy peak) and the charged exciton or trion (T, the lower energy one). Similar excitonic-emission features were previously observed in WS_2 and other binary 2D TMDCs.⁴⁸⁻⁵¹ Such excitonic emissions originate from the direct transition at the K point in the Brillouin zone. There is a switch between the neutral exciton and trion at different Fermi levels.⁴⁸⁻⁵¹ The existence of the trion peak indicates an intrinsic doping of the present sample and these

excitonic-emission features are in good agreement with previous reports.⁵²⁻⁵⁵ The excess electrons in the K valley originate from ionized shallow donors. The neutral excitons and electrons are combined into trions after the optically excited electrons and holes relax into the VBM and CBM. In contrast, the transformation from trion to exciton in the PL spectra is attributed to the dissociation of excess electrons from the molecules.

Fig. 5(b) and (c) show the typical PL spectra recorded at $T = 80$ K and $T = 180$ K for monolayers of WS_2 , $W(S_{0.7}Se_{0.3})_2$, $W(S_{0.5}Se_{0.5})_2$, $W(S_{0.3}Se_{0.7})_2$ and WSe_2 . The two peaks X (blue line) and T (red line) correspond to the exciton and trion emissions obtained by using the Gaussian function fitting. Interestingly, from the PL spectra, we detect an additional electronic transition character (denoted as L, see also Fig. 5(b)) in the lower energy sector under 160 K, but it rapidly quenches with increasing temperature. The transition (L) is attributed to a superposition of the biexciton, trion and localized exciton emission. As shown in Fig. 5(b) and (c), there is an obvious blue shift in the PL emission of $W(S_xSe_{1-x})_2$ alloys at $T = 80$ K and 180 K. At $T = 80$ K, the trions dominate the PL spectra for WS_2 , while the PL intensity of the exciton is stronger than that of the trion at $T = 180$ K. In ternary $W(S_{0.7}Se_{0.3})_2$ alloys, the trions dominate the PL spectra at $T = 80$ K but the main contribution to the PL intensity stems from excitons at $T = 180$ K. The comparison of PL spectra of $W(S_{0.5}Se_{0.5})_2$ MLs exhibit the same mutual relation as in the ternary $W(S_{0.7}Se_{0.3})_2$ alloys. With increasing selenium molar content, the PL intensities of trions and excitons are about the same in $W(S_{0.3}Se_{0.7})_2$. For

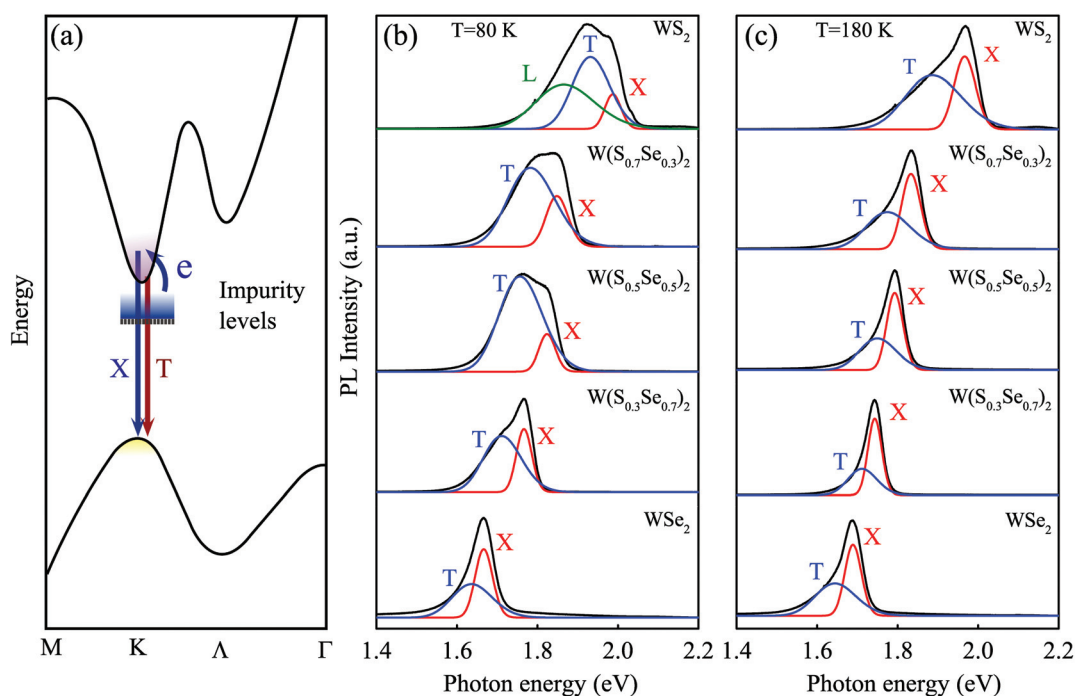


Fig. 5 (a) Schematic illustration of the band structure for monolayer $W(S_xSe_{1-x})_2$ alloys. Typical PL spectra recorded at $T = 80$ K (b) and $T = 180$ K (c) for monolayers of WS_2 , $W(S_{0.7}Se_{0.3})_2$, $W(S_{0.5}Se_{0.5})_2$, $W(S_{0.3}Se_{0.7})_2$ and WSe_2 . The two peaks marked as X and T correspond to the exciton and trion emissions, respectively, obtained by using Gaussian function fitting.

WSe₂, however, the exciton is dominant in the PL spectra at all measured temperatures. The reason is that the amount of ionized shallow donors increases with increasing sulfur molar content, which brings about the excess electron in the K valley. After the optically excited electrons and holes relax into the VBM and CBM, the excess electrons and neutral excitons combined into trions. Thus, the PL intensity of trions increases with the sulfur molar content. As a consequence, sulfur is a contributing factor for the emission of trions.

Fig. 6 presents the evolution of PL spectra as a function of temperature for all monolayers. Note that excitons and trions are detected at all temperatures. In binary WS₂, the PL intensity of the trion is two times stronger than that of the exciton at 80 K. The low energy L peaks rapidly quenches with increasing temperature and cannot be detected in the PL spectra of WS₂ at temperatures above 160 K. The PL intensity of excitons exceeds that of trions in the PL spectra of WS₂ at temperatures above 160 K. The exciton intensity increases to four times stronger than that of trions at 320 K. The common feature observed in the PL spectra of sulfur-rich ternary W(S_xSe_{1-x})₂ alloys is that the trion dominates the PL spectra at low temperatures. With decreasing sulfur molar content, the exciton intensity gradually increases. In selenium-rich ternary W(S_xSe_{1-x})₂ alloys, the PL intensity of the exciton exceeds that of the trion at all measured temperatures.

Fig. 7(a)–(e) present the temperature dependent peak positions of excitons and trions. It is clearly seen that the X and T

resonances in the PL spectra of all W(S_xSe_{1-x})₂ alloys shift to lower energy following the reduction of the band gap with increasing temperature. The PL intensities of exciton and trion emissions as a function of temperature for W(S_xSe_{1-x})₂ alloys are shown in ESI Fig. S5.† The intensities of excitons and trions in ternary W(S_xSe_{1-x})₂ alloys decrease with increasing temperature in general, but with substantial differences for different MLs. In WS₂, the X and T resonances are observed over the entire temperature range. In addition, we can see the optical strength transfer from the L features to the exciton and trion. It implies that the exciton and trion are related to essentially free states, whereas the L features are related to strongly localized states. At elevated temperatures, the transfer of spectral weight from trions to excitons is observed in ternary W(S_xSe_{1-x})₂ alloys with increasing temperature. To get a better insight into this process and to confirm our assignment of excitons and trions, we have analyzed the temperature evolution of the integrated PL intensity ratio of the trion and exciton lines. The most intriguing change is observed in the temperature evolution of the trion to exciton PL intensities ratio (I_T/I_X), as shown in Fig. 7(f). Two regimes of high and low temperature can be distinguished. At low temperatures, below $T \leq 100$ K, the luminescence intensity of trions is much higher than that of excitons for sulfur-rich ternary samples. At temperatures above 100 K, I_T/I_X is less than 1 for ternary W(S_xSe_{1-x})₂ MLs, which suggests that excitons play a significant role in the PL intensity. Therefore, the value of I_T/I_X

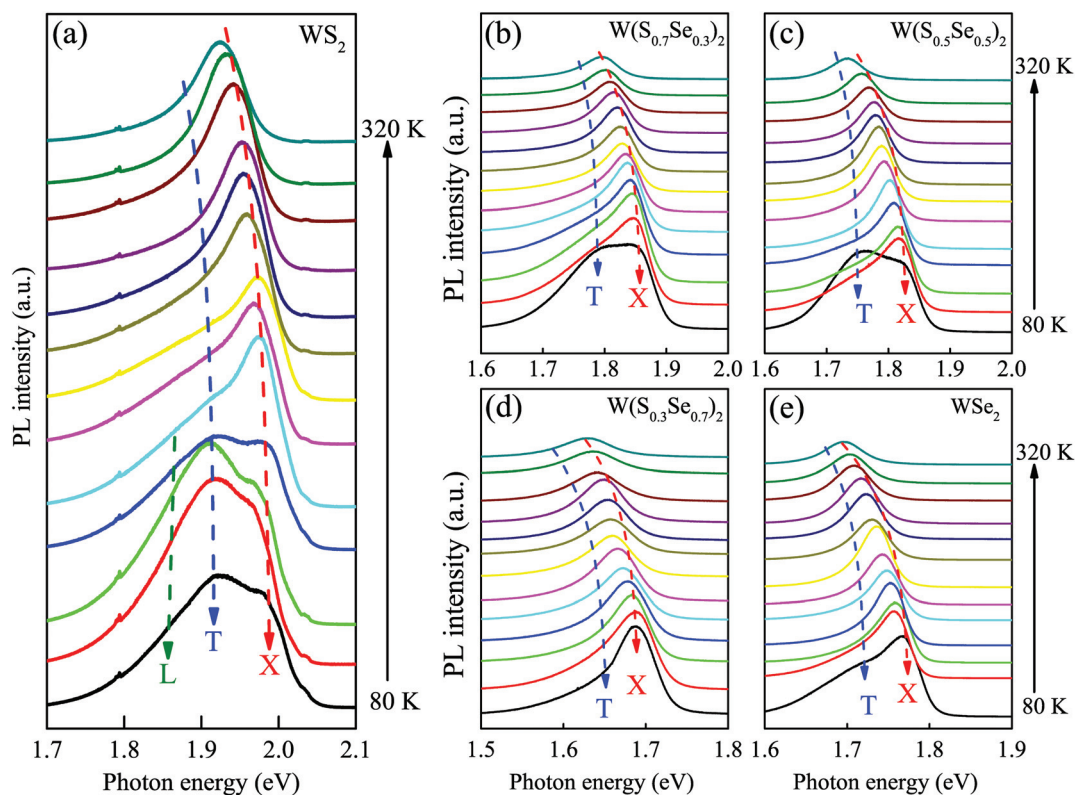


Fig. 6 The temperature evolution of PL spectra for (a) WS₂, (b) W(S_{0.7}Se_{0.3})₂, (c) W(S_{0.5}Se_{0.5})₂, (d) W(S_{0.3}Se_{0.7})₂ and (e) WSe₂.

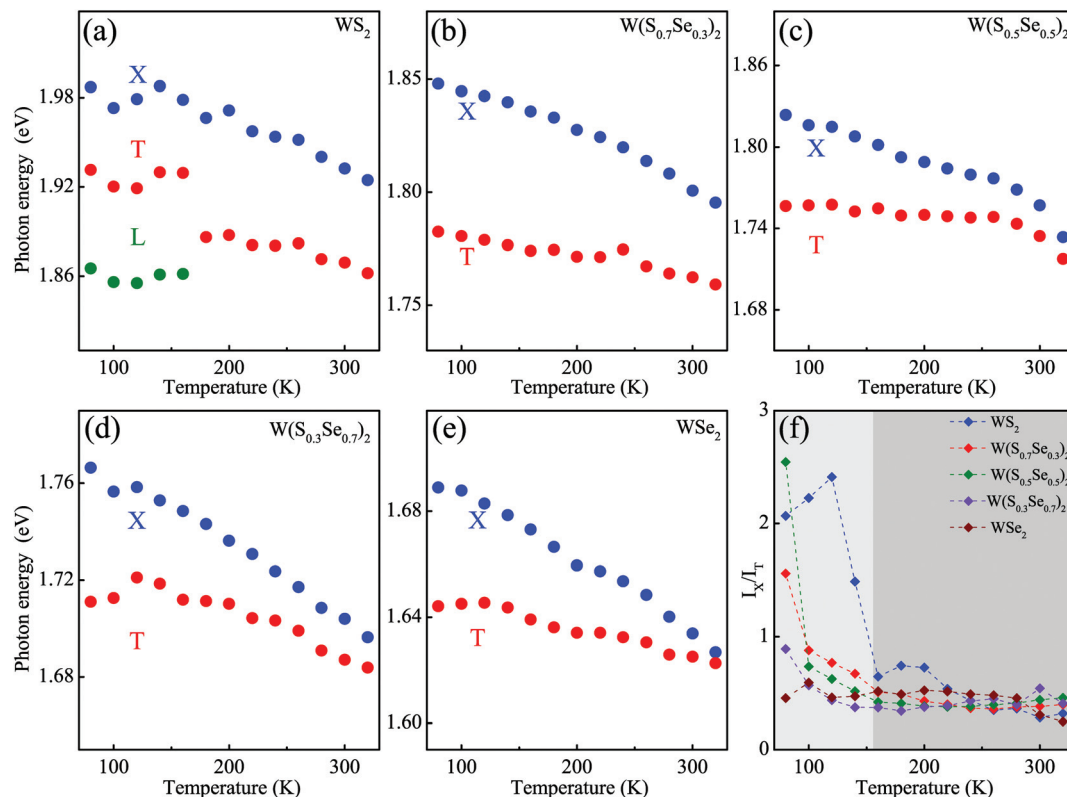


Fig. 7 The exciton (X) and trion (T) emission energy as a function of temperature for monolayer alloy nanosheets: (a) WS₂, (b) W(S_{0.7}Se_{0.3})₂, (c) W(S_{0.5}Se_{0.5})₂, (d) W(S_{0.3}Se_{0.7})₂ and (e) WSe₂. (f) The temperature dependence of the intensity ratio I_T/I_X for trion to exciton in W(S_xSe_{1-x})₂ monolayer.

increases with increasing sulfur molar content. At higher temperatures, the ratio becomes stable. Nevertheless, there is no evident quantitative correlation between $I_T = I_X$ and the sulfur content.

In sulfur-rich ternary W(S_xSe_{1-x})₂ alloys, the trions dominate the PL spectra at low temperatures. At higher temperatures, however, the main contribution to the PL peak stems from excitons. In selenium-rich ternary alloys, excitons are dominant in the PL spectra at all measured temperatures. The reason is that the PL intensities of the excitons and trions are determined by the respective densities of states. At low temperatures, the excess carriers and photo-created electron-hole pairs thermalize into the same locations. The location corresponds to the minima of the potential fluctuations in the monolayer. Therefore, the probability of trion formation increases, which is observed as an increase of the trion emission relative to the exciton emission.

On the other hand, with increasing sulfur molar content in W(S_xSe_{1-x})₂ monolayers, the significant difference in the energy separation of the trion and exciton lines in the PL spectra is related to the remarkable increase of the exciton-trion coupling and a strong difference in the 2D carrier concentration. As the sulfur ratio increases, the A_{1g(S-W-Se)} mode shifts to a higher frequency with increasing intensity. As a consequence, the energy of the out-of-plane A_{1g(S-W-Se)} optical phonon increases, which results in more effective exciton-

trion coupling mediated by this phonon. Also the PL intensity ratio (I_T/I_X) shows an upward trend. Moreover, in selenium-rich W(S_xSe_{1-x})₂ alloys, the carrier concentration is low. The energy separation of the X and T lines is equal to the trion binding energy, it is hard to transform from exciton to trion. In sulfur-rich alloys, during the radiative recombination of an electron-hole pair in a trion complex, an additional electron is excited over the Fermi energy due to the space filling effect. As a result, the two-dimensional electron gas (2DEG) concentration reaches a high level, and the augmentation contributes to the intensity increase of the trion. Therefore, the trion to exciton PL intensity ratio increases with the sulfur content. We attribute these observations to a strong increase of the exciton-trion coupling and to a growth of the 2DEG concentration with increasing sulfur content.

4 Conclusions

In conclusion, we report the one-step CVD growth of single layer W(S_xSe_{1-x})₂ alloys with controlling the relative ratio of sulfur and selenium vapor. The lattice vibration variations from temperature-dependent Raman spectra are attributed to the effect of anharmonicity and thermal expansion. Theoretical calculations confirmed that the band gap value of W(S_xSe_{1-x})₂ alloys increases with the sulfur molar content,

which is in accordance with the experiments. In addition, the PL experiments indicate that the exciton emission behavior of $W(S_xSe_{1-x})_2$ monolayers can be modulated by the sulfur content. At temperatures below 100 K, the PL intensity of trions is much higher than that of excitons for sulfur-rich ternary samples. In selenium-rich ternary alloys, however, excitons are dominant in the PL spectra. These results demonstrate the tuning of different optical transition energies and successful band gap engineering, which can enable spectral tunability for potential optoelectronic applications.

Conflicts of interest

There are no conflicts to declare.

Acknowledgements

This work was financially supported by National Key Research and Development Program of China (Grant No. 2017YFA0303403), Natural Science Foundation of China (Grant No. 61674057, 61504156 and 61227902), Projects of Science and Technology Commission of Shanghai Municipality (Grant No. 18YF1407200, 18YF1407000, 15JC1401600), and the Program for Professor of Special Appointment (Eastern Scholar) at Shanghai Institutions of Higher Learning and the Fundamental Research Funds for the Central Universities.

References

- Q. H. Wang, K. Kolantar-Zadeh, A. Kis, J. N. Coleman and M. S. Strano, *Nat. Nanotechnol.*, 2012, **7**, 699–712.
- J. A. Wilson and A. D. Yoffe, *Adv. Phys.*, 1969, **18**, 193–335.
- K. Mak, C. Lee, J. Hone, J. Shan and T. F. Heinz, *Phys. Rev. Lett.*, 2010, **105**, 136805.
- A. Splendiani, L. Sun, Y. B. Zhang, T. S. Li, J. Kim, C. Y. Chim, G. Galli and F. Wang, *Nano Lett.*, 2010, **10**, 1271–1275.
- A. M. Jones, H. Y. Yu, N. J. Ghimire, S. F. Wu, G. Aivazian, J. S. Ross, B. Zhao, J. Q. Yan, D. G. Mandrus, D. Xiao, W. Yao and X. Xu, *Nat. Nanotechnol.*, 2013, **8**, 634–638.
- A. Mitioglu, P. Plochocka, J. Jadczyk, W. Escoffier, G. Rikken, L. Kulyuk and D. Maude, *Phys. Rev. B: Condens. Matter Mater. Phys.*, 2013, **88**, 245403.
- B. Radisavljevic, A. Radenovic, J. Brivio, V. Giacometti and A. Kis, *Nat. Nanotechnol.*, 2011, **6**, 147–150.
- L. M. Xie, *Nanoscale*, 2015, **7**, 18392–18401.
- X. Duan, C. Wang, Z. Fan, G. Hao, L. Kou, U. Halim, H. Li, X. Wu, Y. Wang, J. Jiang, A. Pan, Y. Huang, R. Yu and X. Duan, *Nano Lett.*, 2016, **16**, 264–269.
- C. Tan and H. Zhang, *Chem. Soc. Rev.*, 2015, **44**, 2713–2731.
- J. S. Ross, S. Wu, H. Yu, N. J. Ghimire, A. M. Jones, G. Aivazian, J. Yan, D. G. Mandrus, D. Xiao, W. Yao and X. Xu, *Nat. Commun.*, 2013, **4**, 1474.
- Y. Zhang, T. Chang, B. Zhou, Y. Cui, H. Yan, Z. Liu, F. Schmitt, J. Lee, R. Moore, Y. Chen, H. Lin, H. Jeng, S. Mo, Z. Hussain, A. Bansil and Z. Shen, *Nat. Nanotechnol.*, 2014, **9**, 111–115.
- D. Xiao, G. Liu, W. Feng, X. Xu and W. Yao, *Phys. Rev. Lett.*, 2012, **108**, 196802.
- W. J. Zhao, Z. Ghorannevis, L. Q. Chu, M. L. Toh, C. Kloc, P. H. Tan and G. Eda, *ACS Nano*, 2012, **7**, 791–797.
- Q. Zeng, H. Wang, W. Fu, Y. Gong, W. Zhou, P. M. Ajiayan, J. Lou and Z. Liu, *Small*, 2015, **11**, 1868–1884.
- P. Rivera, J. R. Schaibley, A. M. Jones, J. S. Ross, S. Wu, G. Aivazian, P. Klement, K. Seyler, G. Klark, N. J. Ghimire, J. Yan, D. G. Mandrus, W. Yao and X. Xu, *Nat. Commun.*, 2015, **6**, 6242.
- H. P. Komsa and A. V. Krasheninnikov, *J. Phys. Chem. Lett.*, 2012, **3**, 3652–3656.
- H. Li, Q. Zhang, X. Duan, X. Wu, X. Fan, X. Zhu, X. Zhuang, W. Hu, H. Zhou, A. Pan and X. Duan, *J. Am. Chem. Soc.*, 2015, **137**, 5284–5287.
- H. Li, X. Duan, X. Wu, X. Zhuang, H. Zhou, Q. Zhang, X. Zhu, W. Hu, P. Ren, P. Guo, L. Ma, X. Fan, X. Wang, J. Xu, A. Pan and X. Duan, *J. Am. Chem. Soc.*, 2014, **136**, 3756–3759.
- C. Tan and H. Zhang, *J. Am. Chem. Soc.*, 2015, **137**, 12162–12174.
- H. Li, X. Wu, H. Liu, B. Zheng, Q. Zhang, X. Zhu, Z. Wei, X. Zhuang, H. Zhou, W. Tang, X. Duan and A. Pan, *ACS Nano*, 2017, **11**, 961–967.
- C. Ge, H. Li, X. Zhu and A. Pan, *Chin. Phys. B*, 2017, **26**, 034208.
- K. He, N. Kumar, L. Zhao, Z. Wang, K. F. Mak, H. Zhao and J. Shan, *Phys. Rev. Lett.*, 2014, **113**, 026803.
- A. Chernikov, T. C. Berkelbach, H. M. Hill, A. Rigosi, Y. Li, O. B. Aslan, D. R. Reichman, M. S. Hybertsen and T. F. Heinz, *Phys. Rev. Lett.*, 2014, **113**, 076802.
- Z. Ye, T. Cao, K. O'Brien, H. Zhu, X. Yin, Y. Wang, S. G. Louie and X. Zhang, *Nature*, 2014, **513**, 214.
- A. S. Pawbake, M. S. Pawar, S. R. Jadhkar and D. J. Late, *Nanoscale*, 2016, **8**, 3008.
- P. Tanndorf, R. Schmidt, P. Bottger, X. Zhang, J. Borner, A. Lietrig, M. Albretch, C. Kloc, O. Gordan, D. R. T. Zahn, S. M. de Vasconcellos and R. Bratschitsch, *Opt. Express*, 2013, **21**, 4908–4916.
- H. R. Gutiérrez, N. Perea-López, A. L. Elías, A. Berkdemir, B. Wang, R. Lv, F. López-Urías, V. H. Crespi, H. Terrones and M. Terrones, *Nano Lett.*, 2013, **13**, 3447–3454.
- J. Jadczyk, J. Kutrowska-Girzycka, P. Kapuściński, Y. S. Huang, A. Wójs and L. Bryja, *Nanotechnology*, 2017, **28**, 395702.
- S. Mouri, Y. Miyauchi and K. Matsuda, *Nano Lett.*, 2013, **13**, 5944.
- Z. Li, R. Ye, R. Feng, Y. Kang, X. Zhu, J. M. Tour and Z. Fang, *Adv. Mater.*, 2015, **27**, 5235.
- K. H. Han, J. Y. Kim, S. G. Jo, C. Seo, J. Kim and J. Joo, *Nanotechnology*, 2017, **28**, 435501.

- 33 P. Hohenberg and W. Kohn, *Phys. Rev.*, 1964, **136**, B864–B871.
- 34 W. Kohn and L. J. Sham, *Phys. Rev.*, 1965, **137**, A1697–A1705.
- 35 D. Vanderbilt, *Phys. Rev. B: Condens. Matter Mater. Phys.*, 1990, **41**, 7892.
- 36 N. J. Ramer and A. M. Rappe, *Phys. Rev. B: Condens. Matter Mater. Phys.*, 2000, **62**, 743–746.
- 37 J. P. Perdew and Y. Wang, *Phys. Rev. B: Condens. Matter Mater. Phys.*, 1992, **45**, 13244–13249.
- 38 M. Staiger, R. Gillen, N. Scheuschner, O. Ochedowski, F. Kampmann, M. Schleberger, C. Thomsen and J. Maultzsch, *Phys. Rev. B: Condens. Matter Mater. Phys.*, 2015, **91**, 195419.
- 39 A. Berkdemir, H. R. Gutiérrez, A. R. Botello-Méndez, N. Perea-López, A. L. Elías, C. Chia, B. Wang, V. H. Crespi, F. López-Urías, J. Charlier, H. Terrones and M. Terrones, *Sci. Rep.*, 2013, **3**, 1755.
- 40 X. Wu, H. Li, H. Liu, X. Zhuang, X. Wang, X. Fan, X. Duan, X. Zhu, Q. Zhang, A. J. Meixner, X. Duan and A. Pan, *Nanoscale*, 2017, **9**, 4707–4712.
- 41 D. J. Late, S. N. Shirodkar, U. V. Waghmare, V. P. Dravid and C. N. R. Rao, *ChemPhysChem*, 2014, **15**, 1592–1598.
- 42 E. S. Zouboulis and M. Grimsditch, *Phys. Rev. B: Condens. Matter Mater. Phys.*, 1991, **43**, 12490–12493.
- 43 S. Tongay, W. Fan, J. Kang, J. Park, U. Koldemir, J. Suh, D. S. Narang, K. Liu, J. Ji, J. Li, R. Sinclair and J. Wu, *Nano Lett.*, 2014, 3185–3190.
- 44 Y. Ma, Y. Dai, M. Guo, C. Niu, J. Lu and B. Huang, *Phys. Chem. Chem. Phys.*, 2011, **13**, 15546–15553.
- 45 E. S. Kadantsev and P. Hawrylak, *Solid State Commun.*, 2012, **152**, 909–913.
- 46 G. B. Liu, W. Y. Shan, Y. Yao, W. Yao and D. Xiao, *Phys. Rev. B: Condens. Matter Mater. Phys.*, 2013, **88**, 085433.
- 47 H. Dery and Y. Song, *Phys. Rev. B: Condens. Matter Mater. Phys.*, 2015, **92**, 125431.
- 48 Y. Ye, X. Dou, K. Ding, D. Jiang, F. Yang and B. Sun, *Nanoscale*, 2016, **8**, 10843.
- 49 A. M. Jones, H. Yu, N. J. Ghimire, S. Wu, G. Aivazian, J. S. Ross, B. Zhao, J. Yan, D. G. Mandrus, D. Xiao, W. Yao and X. Xu, *Nat. Nanotechnol.*, 2013, **8**, 634–638.
- 50 Y. Wang, C. Cong, W. Yang, J. Shang, N. Peimyoo, Y. Chen, J. Kang, J. Wang, W. Huang and T. Yu, *Nano Res.*, 2015, **8**, 2562–2572.
- 51 K. F. Mak, K. L. He, C. Lee, G. H. Lee, J. Hone, T. F. Heinz and J. Shan, *Nat. Mater.*, 2013, **12**, 207–211.
- 52 G. Wang, L. Bouet, D. Lagarde, M. Vidal, A. Balocchi, T. Amand, X. Marie and B. Urbaszek, *Phys. Rev. B: Condens. Matter Mater. Phys.*, 2014, **90**, 075413.
- 53 A. Arora, M. Koperski, K. Nogajewski, J. Marcus, C. Faugeras and M. Potemski, *Nanoscale*, 2015, **7**, 10421.
- 54 A. Singh, G. Moody, K. Tran, M. E. Scott, V. Overbeck, G. Berghäuser, J. Schaibley, E. J. Seifert, D. Pleskot, N. M. Gabor, J. Yan, D. G. Mandrus, M. Richter, E. Malic, X. Xu and X. Li, *Phys. Rev. B: Condens. Matter Mater. Phys.*, 2016, **93**, 041401.
- 55 T. Godde, D. Schmidt, J. Schmutzler, M. Aßmann, J. Debus, F. Withers, E. M. Alexeev, O. Del PozoZamudio, O. V. Skrypka, K. S. Novoselov, M. Bayer and A. I. Tartakovskii, *Phys. Rev. B: Condens. Matter Mater. Phys.*, 2016, **94**, 165301.